Motion Compensation in Histogram-Mode and List-Mode EM Reconstructions: Beyond the Event-Driven Approach

Arman Rahmim, Peter Bloomfield, Sylvain Houle, Mark Lenox, Christian Michel, Kenneth R. Buckley, Thomas J. Ruth, and Vesna Sossi

***Abstract*—With continuous improvements in spatial resolution of positron emission tomography (PET) scanners, small patient movements during PET imaging become a significant source of resolution degradation. This work explores incorporation of motion information into expectation–maximization (EM) reconstruction algorithms. An important issue addressed is the existence of lines-of-response (LORs) corresponding to no actual pairs of detectors and their motion-induced "interaction" with the detectable LORs. An example of this is a scanner design with gaps existing in between the detector heads. It is shown that to properly account for such LORs in histogram-mode and list-mode EM reconstructions, in addition to motion correction of the events, the algorithms themselves *must* be modified. This modification is implemented by including motion-compensated sensitivity correction factors. We are able to demonstrate experimentally that the proposed approach resolves image artifacts that can appear when the conventional purely event-driven motion correction technique is used. An alternate image-space-based method for calculation of motion-compensated sensitivity factors is also derived, applicable in both histogram-mode and list-mode reconstruction tasks, which has the potential of being considerably faster in presence of frequent motion, especially in high-resolution tomographs.**

***Index Terms*—Expectation–maximization (EM) algorithm, histogram-mode, list-mode, motion compensation, positron emission tomography (PET) reconstruction.**

I. Introduction

RECENT developments in three-dimensional (3-D) positron emission tomography (PET) systems have enabled the spatial resolution to reach the 2–3 mm full-width at half-maximum range. With such improvements in spatial resolution, small patient movements during PET imaging become a significant source of resolution degradation. One method to correct for patient movement involves gating of detected events into multiple acquisition frames (MAFs), with the use of an external monitoring system, followed by spatial registration and then summation of reconstructions from the acquired frames [1], [2]. However, the major limitation of the MAF approach is that it is unable to correct for motion during a frame. Subsequently, in the presence of considerable movement, one may need to acquire many *low-count* frames, and subsequently spatially align them, to better correct for patient motion. Lack of an adequate number of acquired events in the individual frames can in turn adversely affect the quality of the final reconstructed image, and an increased number of frames will also lead to increased (histogram-mode) reconstruction times.

Correction of individual lines-of-response (LORs) for motion has alternatively been suggested to achieve optimal motion correction [3]. This is what we shall refer to as the *event-driven approach*, by which it is meant that in either of the histogram-mode or list-mode reconstruction techniques, motion correction is performed by transforming the LORs along which the events *are* measured to where they *would* have been measured had the object not moved. To this end, motion-tracking systems have been used for accurate real-time measurements of position and orientation of the patient (e.g., see [4] for *Polaris*, a system based on optoelectronic position-sensitive detectors). In the histogram-mode approach, this introduces an event-by-event rebinning technique, resulting in motion-compensated sinograms, which are subsequently reconstructed using any of the common reconstruction algorithms [5].

However, it can be argued that the purely event-driven approach can produce image artifacts as compared to a more comprehensive modeling of the image–data relation, as we also demonstrate experimentally in this work. This is because one can observe [6], [7] that certain events that would have been detected in some LORs may have exited the PET scanner (e.g., axially or through detector gaps) undetected due to object motion. Regular reconstruction methods do not employ knowledge of missing data and, therefore, would assume simply that nothing was detected.

One further notes that the converse also requires consideration: upon transformation of certain LORs along which the events are detected to LORs along which the events would have been detected, had the object not moved, the calculated LORs may correspond to no actual detector pairs. In other words, motion can result in some LORs that correspond to undetectable

Manuscript received November 14, 2003; revised July 19, 2004.

This work was supported in part by the Canadian Institute of Health Research, in part by TRIUMF Life Science, in part by the Canada Foundation for Innovation, in part by the Ontario Innovation Trust, in part by the Natural Sciences and Engineering Research Council of Canada University Faculty Award (V. Sossi) and Postgraduate Scholarship B (A. Rahmim) scholarships, and in part by the Michael Smith Foundation for Health Research scholarship (V. Sossi).

A. Rahmim and V. Sossi are with Department of Physics and Astronomy, University of British Columbia, Vancouver V6T 1Z1, BC, Canada (e-mail: rahmim@physics.ubc.ca; vesna@physics.ubc.ca.).

P. Bloomfield and S. Houle are with Vivian M Rakoff PET Centre, Centre for Addiction and Mental Health, Toronto, ON M5T 1R8, Canada (e-mail: peter.bloomfield@camhpet.ca; sylvain.houle@camhpet.ca).

M. Lenox and C. Michel are with CPS Innovations, Knoxville, TN 37932 USA (e-mail: Mark.Lenox@cpspet.com; Christian.Michel@cpspet.com.).

K. R. Buckley and T. J. Ruth are with the University of British Columbia, Vancouver V6T 1Z1, BC, Canada, and also with Triumf, Vancouver V6T 2A3, BC, Canada (e-mail: buckley@triumf.ca; truth@triumf.ca).

Digital Object Identifier 10.1109/TNS.2004.835763

regions to exhibit nonzero probabilities of detection, which also needs to be properly modeled.

Taking these effects into consideration, it is therefore *not* sufficient to merely correct *the events* for motion; rather, one must also modify the algorithms themselves. Sections II and III discuss incorporation of a comprehensive modeling of motion into the histogram-mode and list-mode EM reconstruction. Both sections also describe (Section II-B) an alternative, image-space-based method that has the potential of being considerably faster in presence of frequent motion especially in high-resolution tomographs. Methods and results for experiments on transaxial and axial motion are presented in Sections IV and V.

II. Motion Correction in Histogram-Mode EM Reconstruction

Denoting λ_j^m as the image intensity in voxel j ($j = 1, \ldots, J$) at the mth iteration, and p_{ij} as the probability of an emission from voxel j being detected along LOR i, the histogram-mode expectation–maximization (EM) algorithm is given by

$$\lambda_j^{m+1} = \frac{\lambda_j^m}{\sum_{i=1}^{I} p_{ij}} \sum_{i=1}^{I} p_{ij} \frac{n_i}{\sum_{b=1}^{J} p_{ib} \lambda_b^m} \tag{1}$$

where n_i refers to the number of events detected along LOR i ($i = 1, \ldots, I$). The sensitivity correction factor $s_j = \sum_{i=1}^{I} p_{ij}$ is a summation over all possible measurable LORs ($i = 1, \ldots, I$) and calculates the probability of an emission from voxel j being detected anywhere (constructive summation is performed over those LORs for which $p_{ij} \neq 0$).

In the original algorithms, the measured data n_i were first corrected for attenuation and normalization prior to use in the reconstruction task. However, it was later proposed that these corrections could be included in the algorithm as weighting factors [8]. This can be accomplished by noting that the system matrix $P = (p_{ij})_{I \times J}$ may be more generally written as $P = WG$ where $G = (g_{ij})_{I \times J}$ is the geometric probability of an event generated at voxel j to be detected at LOR i, and the diagonal matrix $W = (w_i)_{I \times I}$ allows a weight to be assigned to each LOR, to account for sensitivity variations. Substituting $p_{ij} = w_i g_{ij}$ into (1) results in the emergence of cancelation of w_i in the back- and forward-projection steps,[1] thus giving

$$\lambda_j^{m+1} = \frac{\lambda_j^m}{\sum_{i=1}^{I} w_i g_{ij}} \sum_{i=1}^{I} g_{ij} \frac{n_i}{\sum_{b=1}^{J} g_{ib} \lambda_b^m}. \tag{2}$$

A. Modification of the Histogram-Mode EM Algorithm

The event-driven histogram-mode motion correction EM scheme (e.g., as elaborated in [9]) consists of reading each list-mode event, producing correction factors (CFs) for the particular event (such as normalization), transforming the LOR in which the event is detected into the LOR in which the event would have been detected had the object not moved, and finally histogramming the event at this calculated LOR along with the application of the CFs. The motion-corrected sinograms, which have also been precorrected for the CFs, are subsequently reconstructed using the unweighted EM algorithm given by (1).

Once a motion-corrected sinogram is obtained, some LORs may be transformed into undetectable LORs (i.e., LORs for which no actual pair of detectors exist). On the other hand, some detectable LORs exhibit fewer counts that they would have, had the object not moved, since corresponding events passed through undetectable LORs. These missing LORs can in principle be located: 1) radially out of the field of view; 2) axially out of the scanner; 3) exceeding the maximum allowed ring difference in the scanner's acquisition mode; or 4) in regions corresponding to gaps in between the detectors.

The first case may be ignored, as it can be safely assumed that the object stays in the radial field of view of the scanner all the time, whereas the second and third cases are especially important in 3-D PET imaging in which small rotations in the object can result in many LOR's to exit the FOV axially or exceed the maximum allowed ring difference, and vice versa. The last possibility is expected to be significant in noncylindrical designs. In the octagonal design of the high-resolution tomograph (HRRT) [10], for instance, gaps existing between the eight detector heads of the scanner occupy over 10% of the sinogram space.

One recently suggested method by Thielemans *et al.* [7] involves scaling of counts recorded in the motion-corrected sinogram bins, where the scale factors are computed using averaging of LOR weighting factors. This can be thought of as a "motion precorrection" technique, which requires consideration of noise enhancement due to small-scale factors division. The authors have then suggested the use of forward-projection of an initial estimate of the image, in combination with or replacing the calculated scale factors (by which the data are divided) when these factors are below a certain threshold.

We now note that such consideration can alternatively be fully addressed by modifying the system matrix itself so as to take motion into account ("motion weighting" of the system matrix as compared to "motion precorrection" of sinograms). This, as we shall demonstrate, results in modification of the sensitivity correction factors and can potentially result in less noise artifacts. This is because, compared to individual scaling of sinogram bins, only the summation of motion-compensation factors over *all* directions is used.[2] Furthermore, as we demonstrate in Section II-B, calculation of such correction can be performed in the image domain, compared to the LOR domain and can thus potentially result in considerable speed-up of the algorithm.

In this regard, we first introduce an invertible operator $\mathcal{L}$ that models the motion of the object by transforming the LOR i along which an event *would* have been detected in absence of any motion, to the LOR i' along which the event *is* detected at time t. An instance of this is shown in Fig. 1, where an event generated from a voxel j, currently located at a position j' due to some transformation $\mathcal{M}(j)$, has been detected along an LOR i', and therefore must be histogrammed along the motion-corrected LOR $i = \mathcal{L}^{-1}(i')$, as is shown.

[1]For any LOR i not corresponding to actual detector pairs, w_i is zero and, therefore, may not be canceled in the numerator and denominator of the EM algorithm; nevertheless, since such an LOR would not receive any counts, i.e., $n_i = 0$, the backprojection summation is automatically done only for those LORs that can correspond to actual detector pairs. This will not be the case in presence of motion, as we discuss later.

[2]This observation is conceptually very similar to relative noise reduction in "weighted" schemes (attenuation/normalization correction) as compared to precorrection schemes. Instead, here in this work, we are concerned with motion correction.

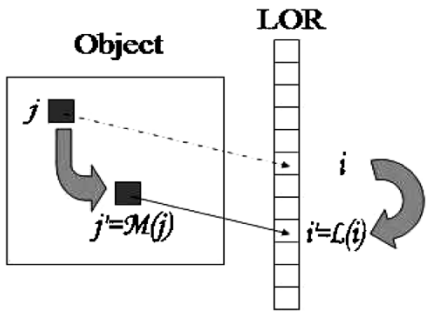

Fig. 1. An event detected at an LOR i' generated in voxel j, which has been translated to voxel $j' = \mathcal{M}(j)$ at time of detection, would have been detected at LOR $i = \mathcal{L}^{-1}(i')$ if the object had not moved.

We next introduce $\tilde{g}^t_{i'j}$ as the motion-dependent geometric probability of detecting an event generated in voxel j along an LOR i' at a given time t. The superscript t indicates knowledge of object orientation and position with respect to the origin of the time axis.[3] Also, defining

$$\delta_i = \begin{cases} 1, & \text{if LOR } i \text{ corresponds to a detector pair} \\ 0, & \text{otherwise} \end{cases} \tag{3}$$

such that $\{i \,|\, \delta_i = 0\}$ is the set of all LORs that correspond to no actual detector pairs, we write

$$\tilde{g}^t_{ij} \equiv g^t_{ij}\delta_i \tag{4}$$

where we use g^t_{ij} to calculate the purely geometric overlap between a voxel j and an LOR i, and δ_i is used to incorporate whether or not the LOR i can be detected by the scanner.

Next, we note that according to the frame of reference of a given voxel j, from a purely geometric point of view, an LOR i' at time t is equivalent to a calculated LOR $i = \mathcal{L}^{-1}_t(i')$ at time $t = 0$, since all LORs at time $t = 0$ have now been transformed by the motion operator $\mathcal{L}_t\{\}$. We thus note that the geometric overlap between a voxel j and an LOR i' at time t, is equal to the overlap it would have had with the calculated LOR i had the object not moved (which is the case at $t = 0$), i.e.,

$$g^t_{i'j} = g^0_{ij} \quad \text{where } i = \mathcal{L}^{-1}_t(i'). \tag{5}$$

Denoting N_i and A_i as the attenuation and detector normalization factors for an LOR i, incorporation of these factors in the presence of motion must now be addressed. In the unweighted scheme, these factors are applied onto the acquired LOR events that are histogrammed into appropriate motion-compensated sinogram bins. Alternatively, in weighted schemes, one or both of these factors are instead used inside the reconstruction algorithm itself. The normalization factor for an LOR i' along which an event is detected is given by the value of $N_{i'}$ for the LOR itself, independent of any motion. However, this is *not* the case for attenuation correction, in which case the factor is given by the value of the attenuation factor at LOR i along which the event would have been detected had the object not moved. This is depicted in Fig. 2.

[3]It is often assumed that the patient does not move between the attenuation scan and the start of the emission scan. Nevertheless, the more general case of having the patient move between the two scans can be treated by motion correction with respect to the time at which the attenuation scan was performed.

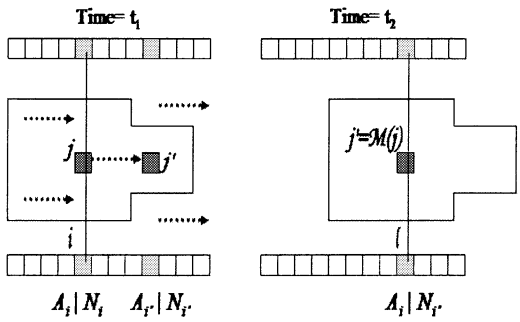

Fig. 2. Event detected at time t_2 along an LOR i', which would have been detected along an LOR i if the object had not moved, has the *same* attenuation correction factor as measured for A_i at time t_1. The normalization correction factor, however, is LOR-specific and changes with motion.

It follows that the weighting factor $w_{i'}$ for any LOR $i' = \mathcal{L}(i)$ can be written as

$$w_{i'} = \begin{cases} N_{i'} & \text{N-weighted} \\ A_i N_{i'} & \text{AN-weighted.} \end{cases} \tag{6}$$

Introducing $\bar{P} = (\bar{p}_{ij})_{I\times J}$ as the motion-compensated system matrix, $\bar{p}_{ij}$ must indicate the probability, for the course of the *entire* scan, that an event generated in object voxel j is finally binned into LOR i. It must therefore incorporate time-weighted probability of detection $(w_{i'}\tilde{g}^t_{i'j})$ contributions from any LOR i' that could record events that would have been detected in LOR i had the object not moved, i.e.,

$$\bar{p}_{ij} = \frac{1}{T}\int_0^T w_{i'}\tilde{g}^t_{i'j}\, dt. \tag{7}$$

It then follows that (7) combined with (4) and (5) can be written as

$$\bar{p}_{ij} = \frac{1}{T} g^0_{ij} \int_0^T w_{i'}\delta_{i'}\, dt. \tag{8}$$

In the AN-weighted scheme, for instance, upon replacing p_{ij} in (1) with $\bar{p}_{ij}$ and dropping the superscript in g^0_{ij} for convenience, one obtains, after cancelations, the following AN-weighted reconstruction algorithm:

$$\lambda^{m+1}_j = \frac{\lambda^m_j}{\bar{s}_j}\sum_{i=1}^{I} g_{ij}\frac{n_i}{\sum_{b=1}^{J} g_{ib}\lambda^m_b} \tag{9}$$

where

$$\bar{s}_j = \frac{1}{T}\sum_{i=1}^{I} g_{ij}A_i \int_0^T N_{i'}\delta_{i'}\, dt. \tag{10}$$

It must be noted that in order to make use of all measured events, the regularly employed sinogram space has to be extended in order to allow histogramming of all motion-compensated LORs, including those that do not correspond to existing detector pairs. As such, the backprojection summation in the numerator of (9) needs to be performed over *all* observed counts and not merely those that correspond to detector pairs (whenever $n_i \neq 0$, it is necessarily the case that $\bar{p}_{ij} \neq 0$ and therefore cancelation of weighting components of $\bar{p}_{ij}$ in the back- and forward-projection steps is valid).

We end this subsection by making an observation: the LOR i (calculated from the measured LOR i') does not typically correspond exactly to the center of a sinogram bin, and an interpolation needs to be performed upon histogramming the event into motion-corrected sinograms. However, as described in the next section, list-mode event coordinates, upon being motion-corrected, can be maintained as continuous variables in list-mode reconstruction, therefore pointing to a potential advantage in terms of inherent accuracy in list-mode reconstruction.

B. An Alternate, Fast Method for Calculation of Sensitivity Factors

For a given voxel j, the task of calculating the motion-weighted sensitivity correction factor $\bar{s}_j$ (10) requires integrating over the entire duration of the scan to derive the properly motion-corrected normalization factors, which are subsequently backprojected along with the attenuation factors. This calculation can, therefore, be very time-consuming for frequent motion in high-resolution scanners. In what follows, we propose an alternative approach in the calculation of motion-weighted sensitivity factors, which can potentially result in very efficient calculation times for high-resolution scanners, as we explain. The technique is applicable to the case where *all* measured LORs are histogrammed and considered in the reconstruction task, including those that do not correspond to actual detector pairs after being corrected for motion.

We make the following very useful observation: at any given time t, calculation of the time-dependent geometric factor $g^t_{i'j}$ can be performed in another way: instead of mapping LOR i' into a motion-corrected LOR i [the approach taken in (5)], one can map the object voxel j to the new voxel j' it has moved to at time t, i.e.,

$$j' \equiv \mathcal{M}_t(j) \tag{11}$$

where $\mathcal{M}_t$ is an image-space-based motion-tracking operator, as depicted in Fig. 1. Mathematically, we have the following identity:

$$g_{ij} = g_{i'j'}. \tag{12}$$

The above relation can lead to considerable speed increase in calculation of s_j for schemes in which data are precorrected for attenuation (i.e., unweighted and N-weighted schemes), as we show here. In the N-weighted scheme, for instance, we have

$$\lambda_j^{m+1} = \frac{\lambda_j^m}{\bar{s}_j} \sum_{i=1}^{I} g_{ij} \frac{n_i/A_i}{\sum_{b=1}^{J} g_{ib}\lambda_b^m} \tag{13}$$

where $\bar{s}_j$ is given by

$$\bar{s}_j = \frac{1}{T}\sum_{i=1}^{I} g_{ij} \int_0^T N_{i'}\delta_{i'}\, dt = \frac{1}{T}\int_0^T \sum_{i=1}^{I} g_{ij} N_{i'}\delta_{i'}\, dt. \tag{14}$$

We next note that the summation over *all* i in the above equation involves consideration of all $i' = \mathcal{L}(i)$, and thus the summation index i can as easily be replaced by i'. Combining this observation with (12) gives

$$\bar{s}_j = \frac{1}{T}\int_0^T \sum_{i'} g_{i'j'} N_{i'}\delta_{i'}\, dt \tag{15}$$

and therefore

$$\bar{s}_j = \frac{1}{T}\int_0^T s_{j'}\, dt$$
$$\text{where } s_j = \textstyle\sum_{i'} g_{i'j} N_{i'}\delta_{i'} = \sum_i g_{ij} N_i \delta_i \tag{16}$$

while noting that s_j is simply the standard sensitivity correction factor that needs to be calculated *only once* for all voxels.

In other words, in the calculation of $\bar{s}_j$ for any voxel j, instead of having to perform time-averaging in the LOR domain, one can do so in the image domain, by evaluating sensitivity factors (which are calculated once for the object at $t = 0$) at voxels j' over time. This corresponds to tracing the motion of voxel j with time, as measured by the motion-tracking system.

Comparing (9) and (13), we make the following observations.

1) The first proposed algorithm does allow for incorporation of attenuation into the system matrix, whereas the latter requires precorrection of the emission data for attenuation. This can result in an increase in image noise (e.g., see [11]), though less increase is expected with better accuracy and statistics in the attenuation and emission measurements. On the other hand, the gain in computation efficiency, especially in full motion compensation, can be very significant, as we shall argue for.
2) The sensitivity correction factor in the first algorithm (10) involves, for each LOR i, a time integral over $N_{i'}\delta_{i'}$ for all LORs i' along which LOR i has come to be aligned due to motion at some point during the scan. In other words, the motion-tracking operator $\mathcal{L}_t\{\}$ must be applied for all the times t considered to every LOR i. Following this time-averaging, the resulting factors are backprojected. In the second algorithm, on the other hand, the sensitivity correction factor (16) is given by a time integral over the standard factors s_j (which is computed once by backprojection of $N_i\delta_i$) for all voxels j' to which voxel j had moved at some point during the scan.

Since with current high-resolution scanners, the LOR domain is typically much larger than the image domain (e.g., in the HRRT, with span 3 and maximum ring difference of 67, one deals with $\sim$470 M LORs whereas one has $256 \times 256 \times 207 \sim 14$ M image voxels), the second approach implies a considerable potential speedup in full motion compensation of motion-corrected sinograms. This speed advantage increases with the number of motion-monitoring intervals (i.e., with degree of "exactness" in monitoring of motion) used in the computation. Nevertheless, scanner, motion and task-dependent studies remain to be performed in order to investigate the tradeoff between image noise (first observation) and computation speed (second observation). As we shall show, this technique will also be applicable to list-mode reconstruction.

III. Motion Correction in List-Mode EM Reconstruction

One must observe that while motion-compensated histogramming involves interpolating the transformation $\mathcal{L}_t^{-1}(i')$ into an actual sinogram bin i, in the case of list-mode reconstruction one can work with LOR coordinates, as compared to rebinned LOR

positions, *thus potentially preserving a higher degree of accuracy* in the reconstruction task. In other words, this improvement results directly from better sampling of the measurement. In this regard, the probability element g_{ij} can be replaced by the operation $\mathcal{G}_j(\mathbf{i})$, which calculates the geometric probability of an event generated at voxel j to occur at LOR $\mathbf{i} = \mathcal{L}_t^{-1}(i')$, a continuous variable, holding the exact coordinates of LOR i' after being motion-corrected.

The list-mode expectation maximization (LM-EM) reconstruction algorithm has been previously formulated by Parra and Barrett [12]. Investigation of the applicability of the algorithm and its accelerated versions are nowadays common in the literature (e.g., see [13]–[15]). Following the list-mode approach, we are able to show in Appendix I that full consideration of motion results in the following EM algorithm:

$$\lambda_j^{m+1} = \frac{\lambda_j^m}{\frac{1}{T}\int_0^T s_j^t dt} \sum_{k=1}^{N} \mathcal{G}_j(\mathbf{i}_k) \frac{1}{\sum_{b=1}^{J} \mathcal{G}_b(\mathbf{i}_k)\lambda_b^m} \tag{17}$$

where $\mathbf{i}_k = \mathcal{L}_t^{-1}(i'_k)$ with i'_k denoting the LOR along which the kth event is detected $(k = 1, \ldots, N)$, and s_j^t is a time-dependent sensitivity correction factor: the probability at time t that an emission from voxel j is detected anywhere.

The overall time-averaged sensitivity correction factor $\bar{s}_j \equiv \frac{1}{T}\int_0^T s_j^t\, dt$ can be calculated on an LOR-domain approach such that any LOR i' is transformed to the corresponding motion-corrected LOR $i = \mathcal{L}_t^{-1}(i')$ for the calculation of time-dependent attenuation and geometric factors, i.e.:

$$\bar{s}_j = \frac{1}{T}\int_0^T s_j^t\, dt = \frac{1}{T}\int_0^T \sum_{i'} g_{ij} A_i N_{i'}\, dt \tag{18}$$

which has also been suggested by Qi and Huesman [16] in order to maximize the log-likelihood function of list-mode data.

Nevertheless, similar to approach of Section II-B, we notice that in the N-weighted scheme, again using (12), one can write

$$\bar{s}_j = \frac{1}{T}\int_0^T \sum_{i'} g_{ij} N_{i'} dt = \frac{1}{T}\int_0^T \sum_{i'} g_{i'j'} N_{i'}\, dt \tag{19}$$

which reproduces (15). Therefore, we propose the following N-weighted algorithm:

$$\lambda_j^{m+1} = \frac{\lambda_j^m}{\bar{s}_j} \sum_{k=1}^{N} g_j(\mathbf{i}_k) \frac{1/A_{i_k}}{\sum_{b=1}^{J} g_b(\mathbf{i}_k)\lambda_b^m} \tag{20}$$

where the overall sensitivity correction factors $\bar{s}_j$ are given by (16).

IV. Methods

Tomograph

Data were acquired on the high-resolution research tomograph. The latest HRRT scanner is a modified version of the scanner described in [10]. The new HRRT scanner has the same octagonal design, but the detector heads are different in that they instead consist of a double 10 mm layer of LSO/LYSO for a total of 119 808 detector crystals (crystal size $2.1 \times 2.1 \times 10$ mm^3). The total number of possible LORs is 4.486×10^9.

Phantoms Used and Measurements Performed

The studies performed in this work involve phantom studies with manual repositioning of the source. Two separate studies were performed, one involving transaxial rotation and the other involving axial translation. The technique described in this paper, however, is *fully applicable to 3-D motion*, which is the case commonly encountered in practice. Upon the availability of a motion-tracking system to us in the near future, the experimental studies will be extended to the general 3-D case. The two studies were as follows.

- *Experiment 1 (Transaxial Rotation):* An F-18 line source was inserted axially into a 70 cm long NEMA phantom (20 cm diameter), placed 4 cm away from and parallel to the central axis of the cylinder. The measured true count rate was 124 k/s with a random fraction of 13%. Three separate frames each of duration 4 min were acquired with the cylinder manually rotated each time by approximately 45° around the z axis.
- *Experiment 2 (Axial Translation of an Extended Source):* Via a technique that allows radioactive printing using a modified standard ink-jet printer [17], we imaged an F-18 "W"-sign ($\sim 4 \times 4$ cm, 4.81 mCi) printed on regular paper. Scans were performed with the source positioned: 1) nearly at center of the scanner (1 min), and also shifted axially by 2) 5 cm (3 min) and 3) 9 cm (3 min) with respect to the first frame.

In both studies, the separate motion frames were then combined into one single frame to study the proposed motion correction techniques. Detector normalization correction factors were obtained from a 12 h scan using a rotating rod source.

Motion Measurement and Compensation: The center of the cylinder used in the first study was expected to have undergone small translations during the manual rotation procedure. In this regard, exact interframe rotations and translations of the phantom were determined by comparison of separate reconstructions for the three frames. The center of the line source reconstructed in each frame was found by means of fitting a Gaussian profile. The relative translational and rotational shifts in between the three centers were then found by means of matching one with another. The motion coordinates (with respect to the first frame) for the second and third frames were found to be: $\Delta X = 3, \Delta Y = 7, \Delta\theta = 40°$, and $\Delta X = 9, \Delta Y = 3, \Delta\theta = 85°$, respectively, where the displacement units (i.e., voxel dimensions) are 1.2 mm.

We denote the LOR coordinate system using (r, θ, z, δ) where r and θ contain the transaxial radial and angular coordinates, while z and δ define the axial position of the center of the LOR and the ring difference between the end-points. In the aforementioned case of transaxial motion, the two elements of the LOR affected by such motion are r and θ. These two follow the relation

$$r = X\cos(\theta) + Y\sin(\theta) \tag{21}$$

for an LOR passing through an image voxel with coordinates (X, Y, Z).

It follows that for an event detected at a given time for an object rotated (counterclockwise) by an angle $\Delta\theta$ with respect to its position at $t = 0$, the appropriate LOR-domain motion operator becomes

$$\mathcal{L}^R(r,\theta,z,\delta) = (r,\theta+\delta\theta,z,\delta) \tag{22}$$

whereas for an object translated by $(\Delta X, \Delta Y)$, we would have

$$\mathcal{L}^T(r,\theta,z,\delta) = (r+\Delta X\cos(\theta)+\Delta Y\sin(\theta),\theta,z,\delta) \tag{23}$$

where the superscripts R and T represent the transaxial rotation and translation operations. Similarly, the equivalent image-domain motion operators are

$$\mathcal{M}^R(X,Y,Z) = (\cos(\Delta\theta)X - \sin(\Delta\theta)Y, \sin(\Delta\theta)X + \cos(\Delta\theta)Y) \tag{24}$$

$$\mathcal{M}^T(X,Y) = (X+\Delta X, Y+\Delta Y). \tag{25}$$

In the axial motion study, the motion operator for an axial shift by ΔZ is given by

$$\mathcal{L}^A(r,\theta,z,\delta) = (r,\theta,z+\Delta Z,\delta) \tag{26}$$

where the superscripts A represent the axial translation operations, while the equivalent image-domain motion operator is

$$\mathcal{M}^A(X,Y,Z) = (X,Y,Z+\Delta Z). \tag{27}$$

The aforementioned LOR-domain and image-domain operators were subsequently used for incorporation into the proposed histogram-mode and list-mode reconstruction methods.

Reconstruction Schemes

Throughout the studies presented in this paper, a span of 3 and maximum ring difference of 67 were used. The motion-compensated histogram-mode (13) and list-mode (20) algorithms proposed in this paper were implemented on the HRRT. Rahmim *et al.* [18] discusses details of implementation and validation of the regular list-mode EM algorithm with random events correction for data acquired on the HRRT, as well as comparison of statistical properties with histogram-mode (3-D ordered subset expectation maximization) reconstruction.

Four schemes were considered in each of the histogram-mode and list-mode tasks: (I) data for the nonmoving phantoms (single phantom position) were first reconstructed. In addition, data for the motion studies were reconstructed (II) without any motion correction, (III) using the conventional purely event-driven technique (i.e., without modification of the sensitivity correction factors), and (IV) with the proposed motion correction algorithms. In histogram-mode reconstruction, two instances of scheme (III) were considered: 1) one in which data allocated to the HRRT detector gaps, after motion corrected histogramming, were ignored and 2) when gap data were not dropped and were used in the reconstruction. The results were subsequently compared using measurement of relative count loss and resolution (line-source study) as well as radial/axial profile comparisons.

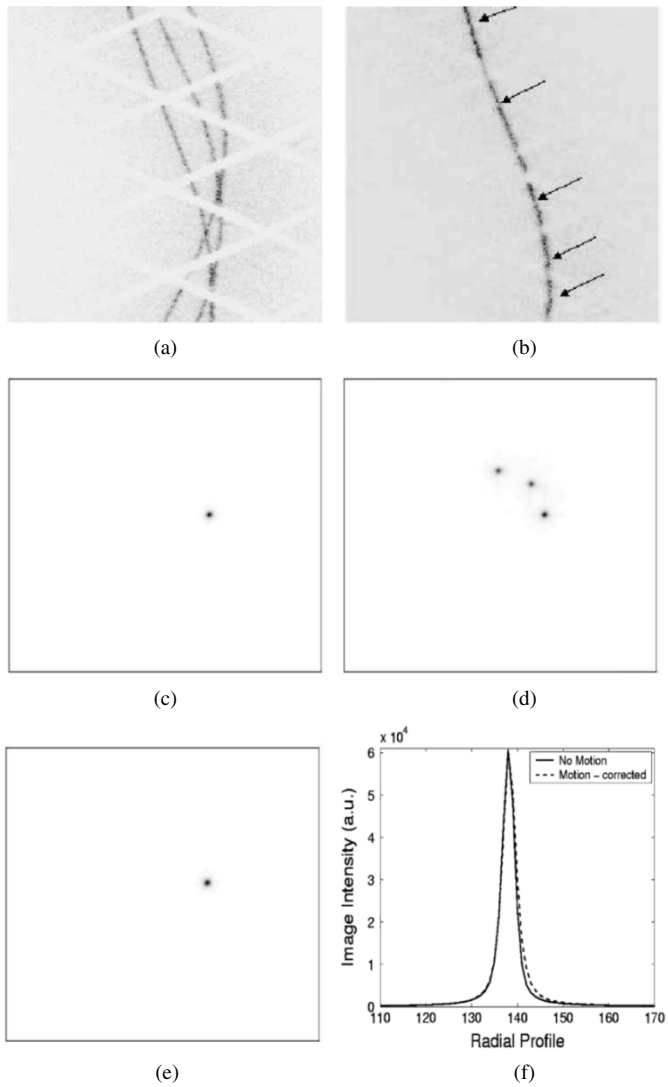

Fig. 3. (Top) Sinograms of a moving line source (a) without and (b) with motion-compensated histogramming. Clearly, upon appropriate histogramming, some counts are histogrammed into bins corresponding to detector gaps (shown by arrows), signifying that they would not have been detected had the object not moved. (Middle) Images reconstructed using histogram-mode algorithm applied to (c) data with no motion and (d) data for motion when reconstructed without motion correction. (Bottom) (e) Image resulting from the proposed reconstruction algorithm given by (13). Radial profiles through this image as well as the one resulting from no motion data are also shown in (f). Three iterations were applied to the data. Direct plane #110 is shown (randomly selected).

V. Results and Discussion

Histogram-Mode Reconstruction

Experiment 1: Fig. 3(a) shows a typical sinogram acquired without any motion correction applied to the line source transaxial motion data. The presence of three distinct sinogram patterns as well as the detector gaps are clearly observable.

Fig. 3(b) shows the resulting sinogram when motion-compensated histogramming is performed. The figure clearly exhibits nonzero counts in certain histogram bins corresponding to detector gaps. Such events, not corresponding to *any* existing detector pairs, are detected due to object motion, as predicted in Section I.

Reconstruction of the motion-compensated sinograms, while ignoring data allocated to detector gaps, using the conventional

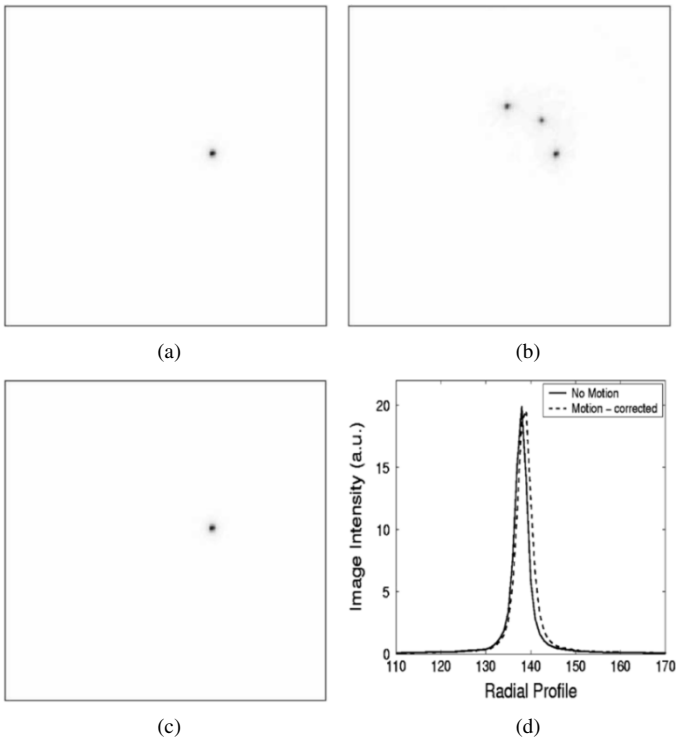

Fig. 4. Images reconstructed using list-mode algorithm applied to (a) data with no motion, as well as data for motion when reconstructed (b) without and (c) with motion correction. (d) Radial profiles through imaged line source in cases (a) and (c) are shown. Three iterations were applied to the data. Plane 110 is shown (randomly selected).

event-driven technique (i.e., scheme (III) while ignoring gap data) was seen to considerably underestimate the image intensity (by 18%), compared to the reference image [scheme (I)]. On the other hand, for the reconstruction schemes (III) (conventional, this time *not* ignoring gap data) and (IV) (proposed), count losses of 2% and 1% were observed, respectively. Furthermore, scheme (III) resulted in a reconstructed image resolution of 4.5 mm, while scheme (IV) showed a resolution of 4.4 mm. In comparison, scheme (I) produced a resolution of 4.1 mm.

Thus, it was observed that ignoring gap data resulted in a reconstructed count bias (plus clearly, discarding of a portion of measured data corresponds to a loss in statistics). Furthermore, schemes (III) and (IV) did not result in noticeably different image qualities. However, as we shall demonstrate, in the axial motion study with an extended object, the two schemes result in significantly different final images.

Fig. 3(c)–(e) shows final images reconstructed using schemes (I), (II), and (IV). Radial profiles through Fig. 3(c) and (e) (i.e., no motion study versus proposed algorithm) are also shown in Fig. 3(f). Comparing the two profiles, a slight broadening of resolution, from 4.1 mm in scheme (I) to 4.4 mm in scheme (IV), was measured which can likely be attributed to the nature of motion measurement we have used (since an accurate motion tracking system is not yet available to us).

List-Mode Reconstruction

Experiment 1: Similar to the previous analysis, images reconstructed from the line source (transaxial motion study) using schemes (I), (II), and (IV) are shown in Fig. 4(a)–(c). The total number of counts in images reconstructed using

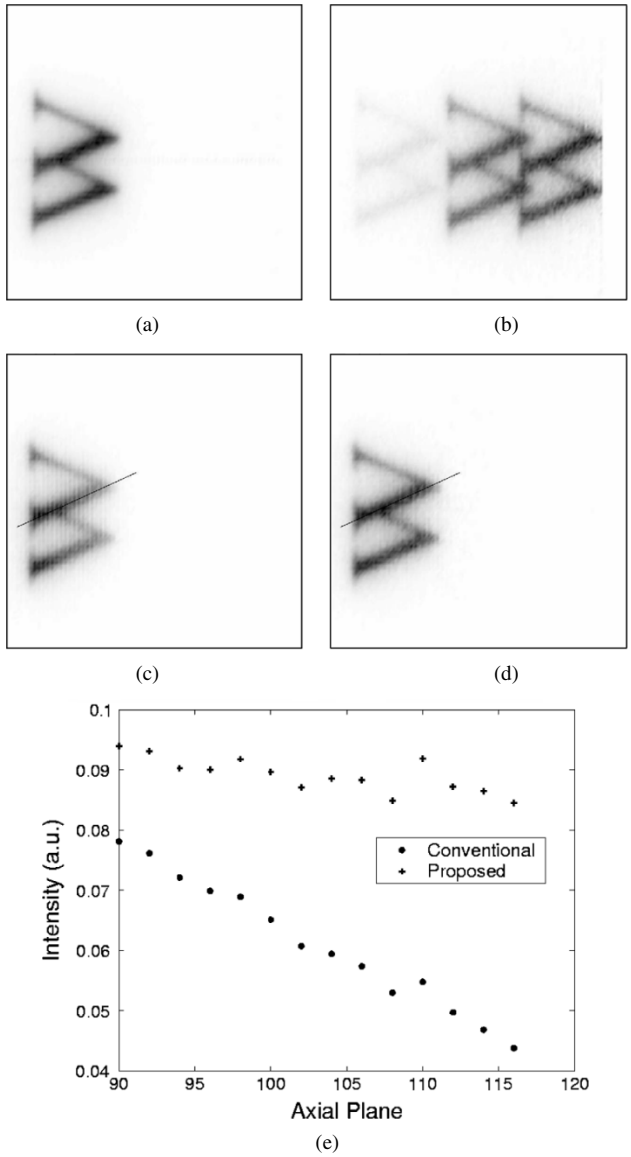

Fig. 5. Images reconstructed for a radioactive printed "W"-sign (coronal view) when (a) no motion is introduced; and with motion (three axial positions: 1 min-3 min-3 min) when (b) no motion compensation, (c) the purely event-driven approach (conventional motion correction), and (d) the proposed algorithm given by (20) are applied to the data. Plots of uniformity profiles drawn through images in (c) and (d) are shown in (e). Five iterations were applied to the data.

the three schemes were confirmed to be within 0.5%. Radial profiles were subsequently drawn through resulting images from schemes (I) and (IV), as shown in Fig. 4(d). Scheme (I) resulted in an imaged resolution of 4.0 mm, while scheme (IV) showed a slightly broadened resolution of 4.3 mm. This we attribute to the nature of motion measurement we have used, as previously mentioned.

However, it was again observed that the conventional scheme (III) did not result in a noticeable decline in image quality. That is, a count loss of 1.5% and resolution of 4.4 mm were measured compared to the proposed scheme (IV), which resulted in a count loss of 0.5% and a resolution of 4.3 mm. This, as in histogram-mode study, is likely due to the transaxial nature of motion in the line source, and as we demonstrate below, the difference is very significant in the next study.

Experiment 2: For the extended source motion study, resulting final images reconstructed using the four schemes (I)–(IV) are shown in Fig. 5(a)–(d). One can clearly observe a nonuniformity in the reconstructed radioactive "W"-sign, when using the conventional scheme (III), whereas this is not the case in the scheme (IV) proposed in this paper. Furthermore, upon drawing profiles through images from schemes (III) and (IV) as shown in the figures, one clearly observes, in addition to the axial nonuniformity artifact visible in the conventional scheme, an overall quantitative loss, measured to be 17% at axial plane 90 (corresponding to the left edge of the sign). Combined with the nonuniformity artifact, the image voxels are underestimated by nearly 50% at the axial plane 150 (the right edge of the sign).

These artifacts can be explained by the fact that in the conventional scheme, the sensitivity factors are not corrected for in accordance with object motion and, therefore, result in overall count underestimation as well as nonuniformity upon motion toward less sensitive regions in the FOV. We have, thus, shown in the new experimental data that the nature of the inaccuracy is *not simply a global scaling* and can result in loss of uniformity, whereas the proposed algorithm achieves better uniformity.

On a last note, we point out that scatter correction is yet to be incorporated into the proposed algorithms in this paper. We are currently evaluating different schemes. One possible approach has already been developed for the HRRT, namely the Watson scatter correction technique [19]. The algorithm is image-based (i.e., computes the scatter contribution using the reconstructed image) and, therefore, has the practical advantage of being directly applicable to images generated using our proposed methods.

VI. Conclusion

This paper has argued for and experimentally demonstrated that the event-driven approach to motion correction, in which one *merely* transforms LORs along which events are detected to LORs along which they would have been detected, can result in image artifacts. The nature of the inaccuracy was shown not to be necessarily restricted to a global scaling and could manifest itself, for instance, as a loss in uniformity. This inaccuracy was attributed to the existence of LORs corresponding to no actual pairs of detectors (e.g., LORs axially out of the FOV) and their "interaction" with the detectable LORs due to motion.

To address the issue, a more comprehensive modeling of the image-data relation was considered. It was subsequently shown that appropriate system matrix modeling of the aforementioned effects into the histogram-mode as well list-mode reconstructions introduced time-weighted sensitivity correction factors. These factors needed to be implemented *in addition* to compensation of the measured events for motion, with the conventional event-driven approach *only* performing the latter.

The resulting motion-compensated sensitivity factors, at first instance, appeared to be potentially very time-consuming to compute for the general case of frequent motion throughout the scan. However, closer inspection of the sensitivity factors revealed that use of attenuation precorrection for the data would allow computation of time-averaging of sensitivity correction factors to be performed in the image domain. This was shown to potentially reduce reconstruction time significantly when correcting for frequent motion especially in high-resolution scanners.

Appendix I
Derivation of List-Mode EM Reconstruction Algorithm With Motion Compensation

In what follows, time of detection will be treated as a continuous random variable, and therefore probability *density* elements, denoted using lowercase p, will be utilized in addition to regular probability elements, denoted here using uppercase P. We define $p(\mathbf{A} \mid D_j, j)$ as the probability density that an event generated in voxel j leads to a measurement $\mathbf{A}$ in the detector, *assuming* the event will be detected (denoted by D_j). The list-mode acquired measurement $\mathbf{A} \in R^d$, where d denotes the dimensionality of the measurement space, can contain such information about the event as, for instance, the LOR i' along which it has been detected, time of detection t and energy.

Parra and Barrett [12] have previously derived the list-mode EM reconstruction algorithm from first principles, which (written in our own notation[4]) is given by

$$\lambda_j^{m+1} = \lambda^m \sum_{k=1}^{N} p(\mathbf{A}_k \mid D_j, j) \frac{1}{\sum_{b=1}^{J} p(\mathbf{A}_k \mid D_b, b)\bar{s}_b \lambda_b^m} \tag{28}$$

where $\mathbf{A}_k$ refers to the coordinates of the kth list-mode event $(k = 1, \ldots, N)$, and $\bar{s}_j$ is defined to be the probability that an event generated from voxel j leads to a measurement anywhere (as we note later, this term must incorporate presence of motion, to correspond to its definition).

We next invoke the relation

$$p(\mathbf{A} \mid D_j, j) = \frac{p(\mathbf{A}, D_j \mid j)}{P(D_j \mid j)} = \frac{p(\mathbf{A} \mid j)}{P(D_j \mid j)} \tag{29}$$

where we have dropped D_j in the numerator of the last term because an event that leads to a measurement $\mathbf{A}$ is necessarily detected. Furthermore, we note that $p(D_j \mid j)$, the probability that an event generated from voxel j is detected (along any LOR and at any time), corresponds exactly to the overall sensitivity correction factor $\bar{s}_j$, i.e.,

$$P(D_j \mid j) \equiv \bar{s}_j. \tag{30}$$

This term, which has no time dependence, must take into account presence of motion throughout the scan, as we show below.

Let us consider any measurement $\mathbf{A} = \{i', t\}$ to indicate the LOR i' and time t at which the measured event is detected. We then have

$$p(\mathbf{A} \mid j) \equiv p(i', t \mid j) = P(i' \mid t, j) p(t \mid j) \equiv P(i' \mid t, j) \frac{1}{T} \tag{31}$$

where under the assumption that image intensity λ_j at any voxel j does not change over duration T of the scan, one notes that $p(t \mid j)$, the probability density that an emission at voxel j has occurred at time t, is a constant (i.e., $p(t \mid j) = (1/T)$). The term $P(i' \mid t, j)$ indicates the probability that an event generated

[4]One needs to carefully note that [12] *does* assume, in the definition of the probability density elements, that the emitted events will be detected (i.e., D_j) but does not explicitly write this out in the derivations.

in voxel j at time t will be detected at LOR i'. This corresponds exactly to the concept of a time-dependent system matrix. It then follows that the probability of detecting (along any LOR and at any time) an event emitted at voxel j is given by

$$\bar{s}_j \equiv \int_0^T \sum_{i'} p(i', t \,|\, j)\, dt = \frac{1}{T} \int_0^T \sum_{\iota} P(i' \,|\, t, j)\, dt. \quad (32)$$

In other words, the probability that a photon emitted at voxel j is detected should include a time average of the time-dependent sensitivity correction factors s_j^t for the course of the scan, i.e.,

$$\bar{s}_j = \frac{1}{T} \int_0^T s_j^t \, dt \quad \text{where } s_j^t \equiv \sum_{i'} P(i' \,|\, t, j). \quad (33)$$

Now, similar to the approach of Section II-A, the attenuation and normalization-weighted probability elements at time t are given by

$$P(i' \,|\, t, j) = A_i N_{i'} \mathcal{G}_j(\mathbf{i}) \quad \text{where } i = \mathcal{L}_t^{-1}(i'). \quad (34)$$

Combining (29), (30), (31), and (34), one has

$$p(\mathbf{A} \,|\, D_j, j) = \frac{A_i N_{i'} \mathcal{G}_j(\mathbf{i})}{T \bar{s}_j} \quad (35)$$

which upon being substituted into (28) results in

$$\lambda_j^{m+1} = \frac{\lambda_j^m}{\bar{s}_j} \sum_{k=1}^{N} \mathcal{G}_j(\mathbf{i}_k) \frac{1}{\sum_{b=1}^{J} \mathcal{G}_b(\mathbf{i}_k) \lambda_b^m} \quad (36)$$

where $\bar{s}_j$, given by (33), is the overall motion-compensated sensitivity correction factor.

ACKNOWLEDGMENT

Part of the computation was performed on the Western Canada Research Grid, for which the authors wish to express gratitude. The authors are also indebted to P. Piccioni for providing his expertise in the radioactive printing experiment.

REFERENCES

[1] Y. Picard and C. J. Thompson, "Motion correction of PET images using multiple acquisition frames," *IEEE Trans. Med. Imag.*, vol. 16, pp. 137–144, Apr. 1997.

[2] R. R. Fulton, S. R. Meikle, S. Eberl, J. Pfeiffer, and C. J. Constable, "Correction for head movement in positron emission tomography using an optical motion tracking system," *IEEE Trans. Nucl. Sci.*, vol. 49, pp. 116–123, Feb. 2002.

[3] M. E. Daube-Witherspoon, Y. C. Yan, M. V. Green, R. E. Carson, K. M. Kempner, and P. Herscovitch, "Correction for motion distortion in PET by dynamic monitoring of patient position," *J. Nucl. Med.*, vol. 31, p. 816, 1990. Abstract.

[4] B. J. Lopresti, A. Russo, W. F. Jones, T. Fisher, D. G. Crouch, D. E. Altenburger, and D. W. Townsend, "Implementation and performance of an optical motion tracking system for high resolution brain PET imaging," *IEEE Trans. Nucl. Sci.*, vol. 46, pp. 2059–2067, Dec. 1999.

[5] P. M. Bloomfield, T. J. Spinks, J. Reed, L. Schnorr, A. M. Westrip, L. Livieratos, R. Fulton, and T. Jones, "The design and implementation of a motion correction scheme for neurological PET," *Phys. Med. Biol.*, vol. 48, pp. 959–978, 2003.

[6] J. Qi and R. H. Huesman, "Correction of motion in PET using event-based rebinning method: Pitfall and solution," *J. Nucl. Med.*, p. 146P, 2002. Abstract.

[7] K. Thielemans, S. Mustafovic, and L. Schnorr, "Image reconstruction of motion corrected sinograms," in *Proc. IEEE NSS and MIC 2002 Conf. Record*, Portland, OR, Oct. 2003.

[8] T. J. Hebert and R. Leahy, "Fast methods for including attenuation in the EM algorithm," *IEEE Trans. Nucl. Sci.*, vol. 37, pp. 754–758, Apr. 1990.

[9] W. F. Jones, "Real-time event stream correction for patient motion in clinical 3-D PET," in *IEEE Nuclear Science Symp. Conf. Record*, vol. 4, 2001, pp. 2062–2064.

[10] K. Wienhard, M. Shmand, M. E. Casey, K. Baker, J. Bao, L. Eriksson, W. F. Jones, C. Knoess, M. Lenox, M. Lercher, P. Luk, C. Michel, J. H. Reed, N. Richerzhagen, J. Treffert, S. Vollmar, J. W. Young, W. D. Heiss, and R. Nutt, "The ECAT HRRT: Performance and first clinical application of the new high resolution research tomograph," *IEEE Trans. Nucl. Sci.*, vol. 49, pp. 104–110, Feb. 2002.

[11] C. Michel, M. Sibomana, A. Boi, X. Bernard, M. Lonneux, M. Defrise, C. Comtat, P. E. Kinahan, and D. W. Townsend, "Preserving Poisson characteristics of PET data with weighted OSEM reconstruction," in *IEEE Nuclear Science Symp. Conf. Record*, vol. 2, 1998, pp. 1323–1329.

[12] L. Parra and H. H. Barrett, "List-mode likelihood: EM algorithm and image quality estimation demonstrated on 2-D PET," *IEEE Trans. Med. Imag.*, vol. 17, pp. 228–235, Apr. 1998.

[13] R. H. Huesman, G. J. Klein, W. W. Moses, J. Qi, B. W. Reutter, and P. R. G. Virador, "List mode maximum likelihood reconstruction applied to positron emission mammography with irregular sampling," *IEEE Trans. Med. Imag.*, vol. 19, pp. 532–537, May 2000.

[14] A. J. Reader, K. Erlandsson, M. A. Flower, and R. J. Ott, "Fast accurate iterative reconstruction for low-statistics positron volume imaging," *Phys. Med. Biol.*, vol. 43, pp. 835–846, 1998.

[15] A. J. Reader, S. Ally, F. Bakatselos, R. Manavaki, R. Walledge, A. P. Jeavons, P. J. Julyan, S. Zhao, D. L. Hastings, and J. Zweit, "One-pass list-mode EM algorithm for high-resolution 3-D PET image reconstruction into large arrays," *IEEE Trans. Nucl. Sci.*, vol. 49, pp. 693–699, Apr. 2002.

[16] J. Qi and R. H. Huesman, "List mode reconstruction for PET with motion compensation: A simulation study," in *Proc. IEEE Int. Symp. Biological Imaging*, 2002, pp. 413–416.

[17] V. Sossi, K. R. Buckley, P. Piccioni, A. Rahmim, M.-L. Camborde, and T. J. Ruth, "Printed sources for positron emission tomography (PET)," in *Proc. IEEE NSS and MIC 2003 Conf. Rec.*, Portland, OR, Oct. 2003.

[18] A. Rahmim, M. Lenox, A. J. Reader, C. Michel, Z. Burbar, T. J. Ruth, and V. Sossi, "Weighted iterative list-mode reconstruction for the high resolution research tomograph," in *Proc. 7th Int. Conf. Fully 3D Reconstruction Radiology Nuclear Medicine*, Saint-Malo, France, 2003.

[19] C. C. Watson, "New, faster, image-based scatter correction for 3D PET," *IEEE Trans. Nucl. Sci.*, vol. 47, pp. 1587–1594, Aug. 2000.